Correlated Heterospectral Lipidomics for Biomolecular Profiling of Remyelination in Multiple Sclerosis

ACS central science

Research Article

Cite This: ACS Cent. Sci. 2018, 4, 39–51

Correlated Heterospectral Lipidomics for Biomolecular Profiling of Remyelination in Multiple Sclerosis

Mads S. Bergholt,[†,‡,§,∥] Andrea Serio,[†,‡,§,∥,⊥] James S. McKenzie,[#] Amanda Boyd,[¶] Renata F. Soares,[#] Jocelyn Tillner,[#] Ciro Chiappini,[†,‡,§,⊥] Vincen Wu,[#] Andreas Dannhorn,[#] Zoltan Takats,[*,#] Anna Williams,[*,¶] and Molly M. Stevens[*,†,‡,§]

[†]Department of Materials, Imperial College London, London SW7 2AZ, United Kingdom

[‡]Department of Bioengineering, Imperial College London, London SW7 2AZ, United Kingdom

[§]Institute of Biomedical Engineering, Imperial College London, London SW7 2AZ, United Kingdom

[#]Computational and Systems Medicine, Imperial College London, London SW7 2AZ, United Kingdom

[¶]MRC Centre for Regenerative Medicine, University of Edinburgh, Edinburgh EH16 4UU, United Kingdom

Supporting Information

ABSTRACT: Analyzing lipid composition and distribution within the brain is important to study white matter pathologies that present focal demyelination lesions, such as multiple sclerosis. Some lesions can endogenously re-form myelin sheaths. Therapies aim to enhance this repair process in order to reduce neurodegeneration and disability progression in patients. In this context, a lipidomic analysis providing both precise molecular classification and well-defined localization is crucial to detect changes in myelin lipid content. Here we develop a correlated heterospectral lipidomic (HSL) approach based on coregistered Raman spectroscopy, desorption electrospray ionization mass spectrometry (DESI-MS), and immunofluorescence imaging. We employ HSL to study the structural and compositional lipid profile of demyelination and remyelination in an induced focal demyelination mouse model and in multiple sclerosis lesions from patients *ex vivo*. Pixelwise coregistration of Raman spectroscopy and DESI-MS imaging generated a heterospectral map used to interrelate biomolecular structure and composition of myelin. Multivariate regression analysis enabled Raman-based assessment of highly specific lipid subtypes in complex tissue for the first time. This method revealed the temporal dynamics of remyelination and provided the first indication that newly formed myelin has a different lipid composition compared to normal myelin. HSL enables detailed molecular myelin characterization that can substantially improve upon the current understanding of remyelination in multiple sclerosis and provides a strategy to assess remyelination treatments in animal models.

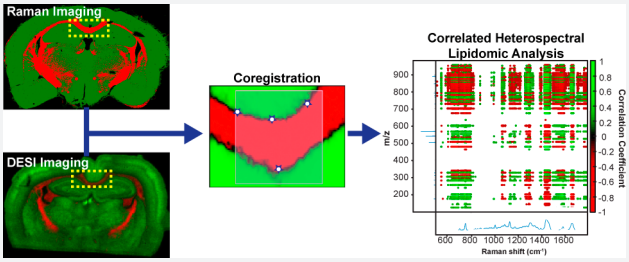

INTRODUCTION

Multiple sclerosis is a degenerative condition of the central nervous system, characterized by multifocal inflammatory demyelinating lesions. Demyelination of axons compromises the efficiency of saltatory conduction of electrical impulses[1] and reduces metabolic support[2,3] to the underlying axon, causing increased susceptibility to degeneration.[4,5] Remyelination occurs to some extent in many multiple sclerosis lesions, but this process varies between individual lesions and different patients and over the disease course,[6−9] and remyelination inevitably fails over time.[6] Much research is now focusing on the discovery of therapies that enhance remyelination, aiming to reduce axonal degeneration and the subsequent progressive accumulation of disability in patients.

To find an effective pro-remyelinating therapy, it will be crucial to reliably and quickly analyze the amount of myelination in different lesions at the molecular level in animal models of demyelination and remyelination and, ideally, in living multiple sclerosis patients. Furthermore, it is important to distinguish between myelin that has been replaced (remyelinated myelin) and normal myelin. Currently, to detect and quantify remyelination in tissue samples, whether from animal models or multiple sclerosis patient brain tissue samples, researchers generally use histochemical staining (e.g., Luxol fast blue staining), or immunohistochemistry using antibodies targeted against myelin proteins such as myelin basic protein (MBP), or proteolipid protein,[10] but do not assess lipids which are the main component of myelin. The current gold standard for more comprehensive quantification of remyelination in a lesion, especially in animal models of demyelination, is to use electron microscopy to directly observe the number of myelinated axons and myelin sheath thickness, as remyelinated myelin is usually thinner than normal myelin.[11,12] This method, however, does not examine the molecular content. In general, conventional methods for assessing myelin require destructive

Received: August 19, 2017
Published: December 27, 2017

DOI: 10.1021/acscentsci.7b00367
ACS Cent. Sci. 2018, 4, 39−51

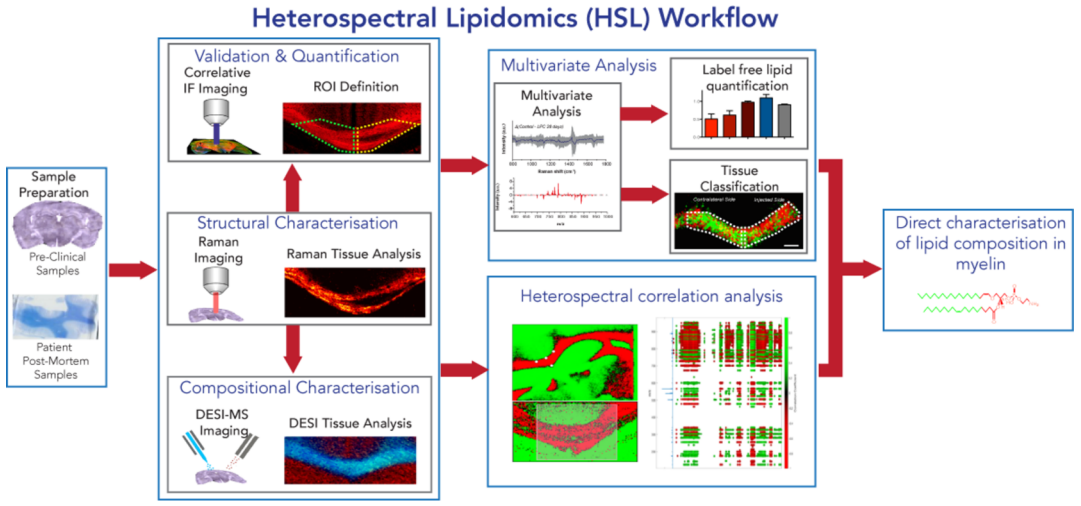

Figure 1. Heterospectral lipidomics for analysis of myelination. Heterospectral lipidomics (HSL) workflow for studying myelin in animal models and human tissue.

sample preparation (e.g., fixation, antigen retrieval, or delipidation for antibody staining) and are poor at assessing the lipid composition of myelin.

Therefore, most myelin characterization performed so far has focused on myelin proteins, rather than on the lipid components. We know that changes in myelin protein composition negatively impact axonal survival[13,14] and that subtle changes in protein composition (e.g., Claudin-11) may occur in myelin after remyelination which may be similar to that occurring in aging myelin.[15] As these proteins are membrane bound or lipid anchored, alterations in the lipid composition of myelin in disease or repair may also be important. However, as yet, we have not identified any studies addressing the lipid composition of newly formed myelin after demyelination in either models or humans, perhaps as it is extremely challenging to identify spatially resolved lipids in a focal lesion with current techniques. Yet, a full lipidomic characterization of myelin and remyelinated myelin may provide additional information to help better understand diseases such as multiple sclerosis.

In recent years, several optical techniques have been introduced for myelin characterization such as Fourier transform infrared spectroscopy[16,17] as well as stimulated Raman spectroscopy and coherent anti-Stokes Raman spectroscopy.[18,19] Spontaneous Raman spectroscopy techniques can acquire the full complement of biomolecular vibrational information and identify a wealth of biomolecules (i.e., specific biomolecular structures and conformations of proteins, lipids, nucleic acids, etc.) in tissue, without labeling, using endogenous molecules as a contrast mechanism. Importantly, lipids are the major components in myelin sheaths, and these are particularly strong Raman scatterers, making this vibrational imaging technique uniquely suited to elucidate the complex structure of myelin.[19,20] Since Raman spectroscopy is nondestructive and requires no tissue processing, it can combine with other complementary techniques such as mass spectrometric (MS) surface analysis by secondary ion MS (SIMS), desorption electrospray ionization (DESI) or matrix-assisted laser desorption−ionization MS (MALDI).[21−23] While Raman spectroscopy provides vibrational structural information, mass spectrometry enables molecular identification. Although several studies have reported on both techniques, their heterospectral analysis has not yet been realized, mainly due to the computational complexity associated with coregistration of the hyperspectral data sets. Recently, a partial correlative approach was developed for Raman spectroscopy and MALDI using neighboring tissue sections as a new analytical strategy.[24] While MALDI provides information on a broad range of species from metabolites to proteins, it requires substantial sample preparation and presents limited capabilities in the detection and characterization of species in the low m/z region associated with lipids.[25] In contrast, DESI-MS is an ambient technique that requires virtually no sample preparation, can be performed on glass slides compatible with confocal Raman spectroscopy thereby enabling true correlative analysis, and is particularly suited to study lipids.[26] This makes it an optimal technique for studying the molecular composition of myelin. Raman spectroscopic imaging (for structural information) and DESI-MS imaging (for specific compositional profiling) can provide two highly complementary techniques for lipid characterization of brain tissue.

In this study, we developed a new correlated heterospectral lipidomics (HSL) imaging strategy for molecular characterization and quantification of remyelination based on correlative Raman spectroscopy and DESI-MS analysis, validated with immunolabeling for specific myelin proteins. We developed a comprehensive computational library for pixelwise coregistration of Raman, DESI-MS hyperspectral data sets and immunofluorescence images. We harnessed the wealth of Raman and DESI-MS hyperspectral data to generate a heterospectral map for correlation of the biomolecular structure and composition of tissue *ex vivo*. Multivariate regression analysis enabled Raman-based assessment of highly specific lipid subtypes in complex tissue for the first time. We applied the HSL approach to the characterization of remyelination in a mouse model of focal demyelination as well as *postmortem* brain samples with multiple sclerosis. Here we show for the first time differences in lipid composition not only between demyelinated and normal brain tissue but, more importantly, between remyelinated tissue and normal myelinated tissue.

RESULTS

Heterospectral Lipidomics (HSL) Workflow. Our computational analysis framework takes full advantage of

DOI: 10.1021/acscentsci.7b00367
ACS Cent. Sci. 2018, 4, 39−51

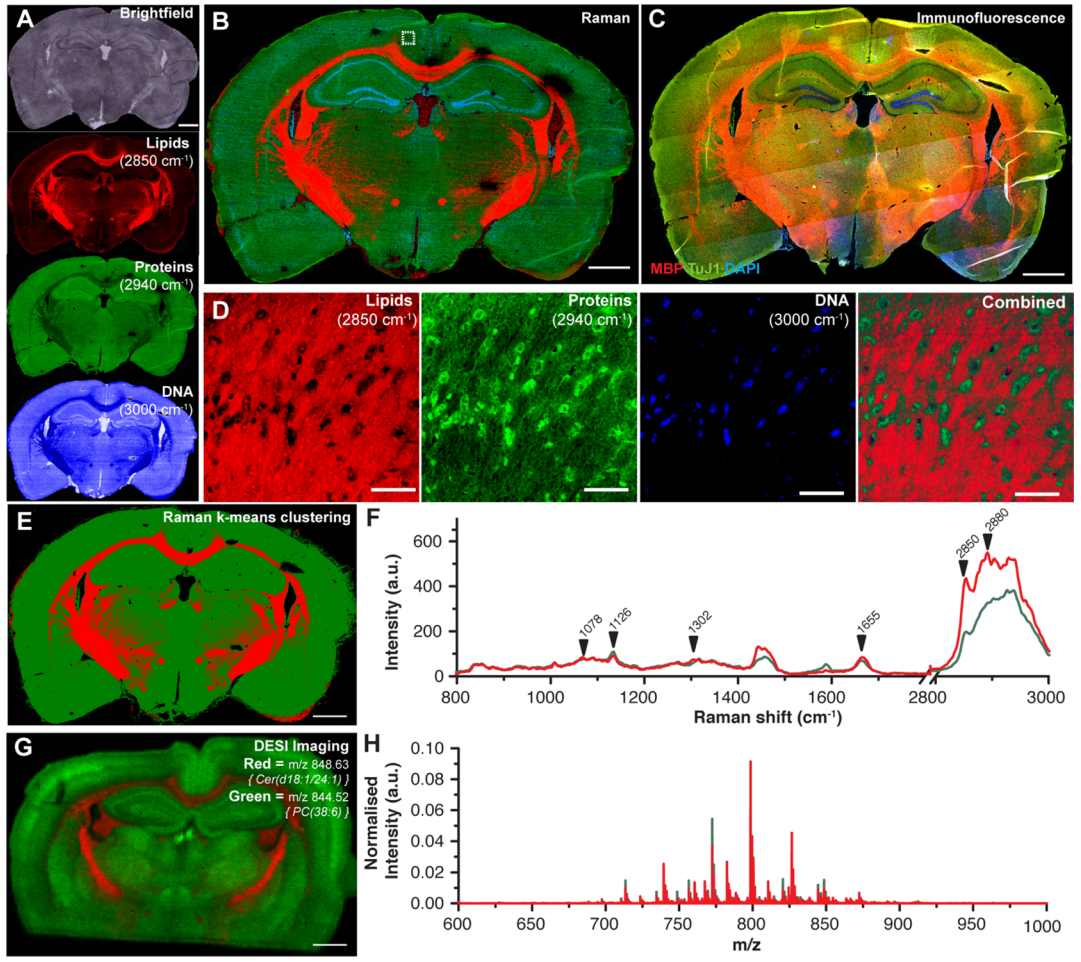

Figure 2. Raman spectroscopy, desorption electrospray ionization mass spectrometry, and immunofluorescence imaging of a mouse brain. (A) Images of a coronal mouse brain section showing brightfield image and Raman spectroscopy images associated with bands of lipids centered at 2850 cm^{-1}, proteins at 2940 cm^{-1}, and DNA at 3000 cm^{-1}. Each spectrum in this image was baseline corrected with a linear polynomial and normalized in the range 2780−3050 cm^{-1}. Scale bar: 1 mm. (B) The Raman overlay of lipids, proteins, and DNA. Scale bar: 1 mm. (C) Representative staining for myelin bound protein (MBP), Tuj1 (class III beta-tubulin), and 4′,6-diamidino-2-phenylindole (DAPI). Scale bar: 1 mm. (D) High resolution microscopic Raman images of a region of interest in the mouse brain (200 × 200 μm) showing Raman spectroscopy peaks associated with lipids (2885 cm^{-1}), proteins (2940 cm^{-1}), and DNA (3000 cm^{-1}). Scale bar: 40 μm. (E) *k*-means clustering (n = 2 clusters) showing distinct signatures of the brain tissue. (F) Representative mean Raman spectra associated with the two *k*-means clusters. (G) DESI-MS imaging of the major myelin showing separation between gray and white matter based on m/z 848.63 and m/z 844.52 respectively, putatively assigned to Cer(d18:1/24:1) and PC(38:6). (H) Representative mean DESI-MS spectra of gray and white matter (respectively in green and red).

Raman-based molecular structural information with subsequent lipid composition information provided by DESI-MS imaging (Figure 1). The data preprocessing, coregistration, and multivariate analysis of the hyperspectral Raman and DESI-MS images were combined into a comprehensive computational library in the Matlab environment (see Materials and Methods). This allows us to generate a heterospectral map for characterizing the lipidomics of brain tissue based on the complementary structural and compositional information. The heterospectral map can directly be used for spectral interpretation including band assignment of overlapping Raman peaks. Further, to enable Raman-based molecular assessment of specific lipid species in the complex tissue we demonstrate here the multivariate regression of the Raman spectra (vibrational information) against the mass spectra (molecular weight distribution information) using partial least-squares (PLS) analysis.

We have also analyzed the two modalities independently using multivariate statistical analysis. For quantitive myelin analysis of the Raman data set, we deconvolved the tissue Raman spectrum into myelin lipids and nonmyelinated tissue using multivariate curve resolution (MCR).[27,28] We used the ratio of myelinated and nonmyelinated tissue from the MCR to generate a Raman myelination index (RMI) representing the relative amount of myelin in each sample. To confirm the fidelity of the RMI-based myelin quantification we used immunofluorescence for identifying myelin proteins, as a well-established reference technique (Figure 1). For classification of the Raman spectra and DESI mass spectra we employed the established PLS discriminant analysis (PLS-DA) and maximum margin criterion linear discriminant analysis (MMC-LDA), respectively.[29]

Heterospectral Raman Spectroscopy, DESI-MS, and Immunofluorescence Imaging of Brain Tissue Samples. We first acquired a high-resolution Raman spectroscopic image (~9500 × 6100 μm, spatial resolution of ~10 μm) of a normal coronal brain section (Figure 2A) containing over 930 million data points (each pixel contains 1600 data points). Each Raman

DOI: 10.1021/acscentsci.7b00367
ACS Cent. Sci. 2018, 4, 39−51

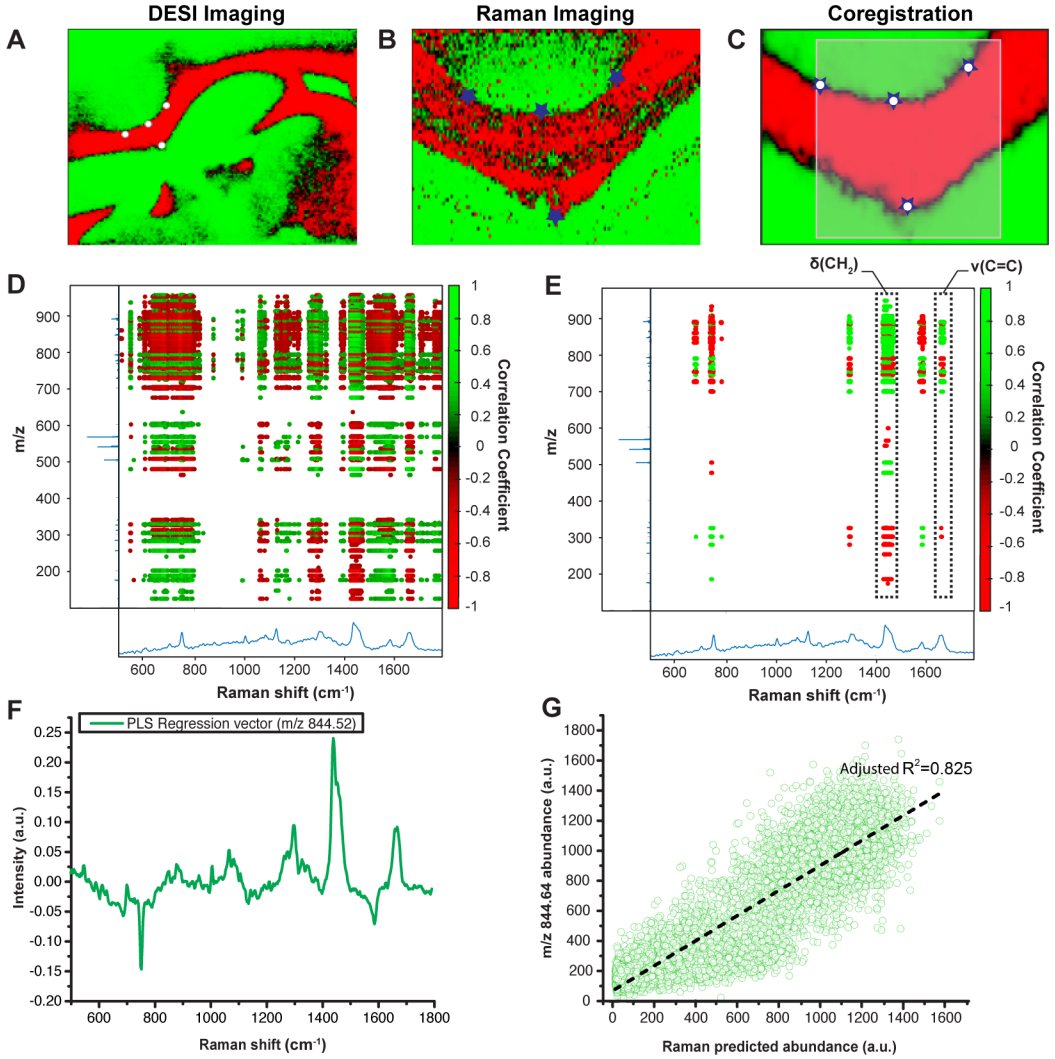

Figure 3. Pixelwise heterospectral Raman and DESI-MS. Heterospectral correlation maps between Raman and DESI-MS hyperspectral images (negative mode). (A) DESI ion image showing the location of the fiducial markers with corresponding locations in panel B marked for the Raman ion image. (C) The transformed DESI image with a region of interest showing the pixels used for correlative analysis of DESI and Raman data. (D) Threshold of heterospectral correlation set at 0.2. (E) Threshold of correlation coefficient set at 0.7. In both D and E the correlations with $p > 0.05$ were discounted. (F) PLS regression vector showing that the model is sensitive to the lipid specific peaks m/z 844.52. (G) PLS regression showing a predictive model with an adjusted R-square of 0.825.

spectrum was collected with an acquisition time of 0.4 s. Imaging the distinct lipid markers centered at 2850 cm^{-1} (symmetric CH_2 stretching of lipids), protein content 2940 cm^{-1} (CH_2 stretchings), and DNA at 3000 cm^{-1} enabled visualization of central nervous system (CNS) structural features (Figure 2A,B,D). Major myelinated structures including the corpus callosum and striatal fiber bundles could clearly be demarcated from a background of axonal lipids. Representative mean Raman spectra (identified using k-means clustering, n = 2 clusters) are shown in Figure 2E,F with noticeable Raman peaks listed in Supplementary Table S1. We also constructed a spectral library of some of the major proteins and lipids associated with myelin and CNS by collecting Raman spectra of each purified lipid or recombinant protein, from commercially available sources (Supplementary Figure S1). Analysis of the single myelinated tissue component spectra confirms that the molecules largely contributing to myelinated tissue spectra are lipids, including cerebroside, cholesterols, sphingomyelin, phosphatidylcholine, and, to a much lesser degree, proteins (Figure 2F).

We then confirmed the molecular specificity of Raman spectroscopy by correlative immunofluorescence for MBP (myelin basic protein), TUJ1 (beta3 tubulin), and DAPI (nuclei) (Figure 2C). This shows that Raman spectroscopic imaging provides highly detailed information about different biomolecular features in the tissue, down to the cellular level (Figure 2D), similarly to conventional immunolabeling techniques.

Since the immunostaining is inherently destructive, in a sequential brain section we performed DESI-MS (spatial resolution of ~50 μm) and imaged the major myelin markers based on m/z 848.63 and gray matter, based on m/z 844.52, which were putatively assigned to Cer(d18:1/24:1) and PC(38:6) respectively (Figure 2G). Representative mass spectra of white and gray matter are shown in Figure 2H. These results show it is possible to image lipids in myelin using both Raman spectroscopic structural information and DESI-MS for specific compositional profiling.

We finally showed that Raman spectroscopy and DESI-MS can be performed sequentially on the same tissue sample. We

DOI: 10.1021/acscentsci.7b00367
ACS Cent. Sci. 2018, 4, 39−51

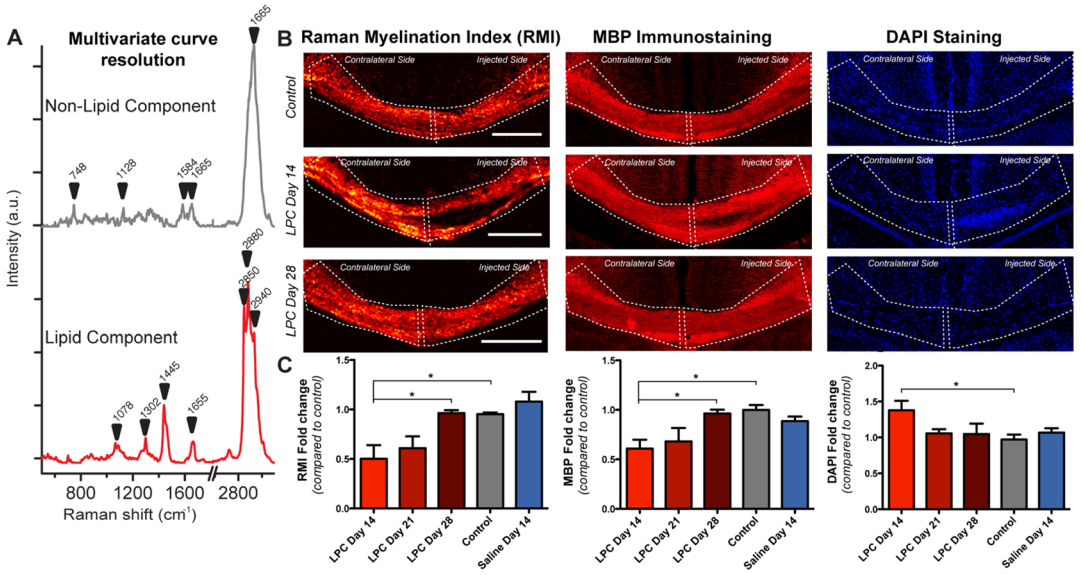

Figure 4. Quantification of remyelination in a mouse model using RMI. (A) MCR deconvolved pure components representing demyelinated tissue and myelinated tissue with marked signatures for lipids. The ratio of myelinated to demyelinated tissue was used to form the RMI (most relevant peaks highlighted). (B) Images of RMI, correlative immunostaining for MBP, and 4′,6-diamidino-2-phenylindole (DAPI) staining for control, 14 and 28 days post LPC injection. Scale bar: 500 μm. (C) Mean RMI, MBP, and DAPI fold change ± 1 standard error compared to contralateral hemisphere for 14, 21, and 28 days post injection. Also shown are control (nontreated) and saline injected (day 14). * indicates $p < 0.05$ (one-way ANOVA: for RMI fold change $p = 0.006$, Newman−Keuls post-test LPC day 14 vs day 28/control/saline $p < 0.05$; for MBP fold change $p = 0.002$, Newman−Keuls post-test LPC day 14 vs day 28/control $p < 0.05$).

performed direct HSL analysis by pixelwise coregistering the Raman and DESI-MS hyperspectral image using our developed computational framework (Figure 3A−C), focusing on the corpus callosum (Supplementary Figure 2 shows the anatomical structure within the context of the brain section). This allowed us to generate a heterospectral DESI-MS and Raman correlation map that enables the assignment of structural features detected by vibrational spectroscopy to individual molecular species detected by mass spectrometry (Figure 3D,E). Generally, the data showed a high degree of correlation between Raman vibrational peaks associated with the myriad of different lipids. For instance, we found the strongest positive correlation for the CH_2 deformation vibrations near 1440 cm^{-1} and ν(C═C) at 1650 cm^{-1} and mass peaks at m/z 844.52 suggestive of PC(38:6) lipids (correlation coefficient >0.79 for 1440 cm^{-1}, and correlation coefficient >0.56 for 1650 cm^{-1}). This technique also revealed the subtle and apparently buried Raman peaks that cannot be assessed using Raman spectroscopy alone (e.g., weak C−C stretching bands of lipids in the range 1050−1200 cm^{-1}). Conversely, as expected, the most common protein Raman peaks (e.g., the amide III at 1245 cm^{-1} and highly specific phenylalanine Raman peak near 1004 cm^{-1}) correlated poorly with any of the masses. Interestingly, we also observed negative correlations, in particular for the cytochrome resonance Raman peaks of mitochondria (e.g., near 748 and 1585 cm^{-1}). This is likely because white matter contains an abundance of lipids and therefore relatively fewer mitochondria per volume compared to gray matter. Hence, once a single heterospectral map has been developed for a specific tissue type, this can improve spectral interpretation including band assignment of overlapping Raman peaks and allows us to better understand the compositional origin of overlapping Raman peaks in biological complex samples and vice versa for DESI-MS imaging. Since excellent correlation could be achieved, we then performed a PLS multivariate regression of the Raman spectra against the mass spectra (see Materials and Methods). As an example we regressed the Raman spectrum against the m/z 844.52 PC(38:6). The regression vector showed highly specific lipid peaks indicating specificity to phosphatidylcholine (Figure 3F). The regression analysis showed that a highly linear relationship could be established (adjusted R^2 = 0.825) (Figure 3G). Assuming—in a first approximation—linearity of the mass spectrum with concentration, this Raman-based model can serve as a predictor of specific lipid species in complex tissue. These results represent a novel demonstration of lipidomic profiling using complementary spectral modalities based on both structural and biomolecular information.

Heterospectral Lipidomics in a Mouse Model. We first applied our HSL characterization to tissue from a mouse model of demyelination as a proof of principle. We assembled correlative images that incorporate specific immunolabeling for MBP with the Raman k-mean clustering images (n = 2 clusters) for the lipid component using ImageJ and found that the lipid-rich component identified correlated well with the MBP+ myelinated areas in the tissue (Supplementary Figure S2).

We then used a mouse model of focal demyelination based on stereotactic injection of lysophosphatidylcholine (LPC) into the mouse corpus callosum.[11] We acquired high resolution Raman spectroscopic images (n = 15) of the corpus callosum in fixed coronal brain sections. We analyzed sections taken from days 14, 21, and 28 after LPC injection in order to cover the whole process from demyelination to complete remyelination (day 28 post injection). We used two controls: noninjected mice (control) and mice injected with saline only at day 14 post injection (i.e., with no demyelination). We then calculated the RMI (see Materials and Methods) at different time points post LPC injection by deconvolving the myelinated tissue spectrum using MCR (Figure 4A). Figure 4A displays two pure MCR basis spectra essentially representing myelin lipids and

DOI: 10.1021/acscentsci.7b00367
ACS Cent. Sci. 2018, 4, 39−51

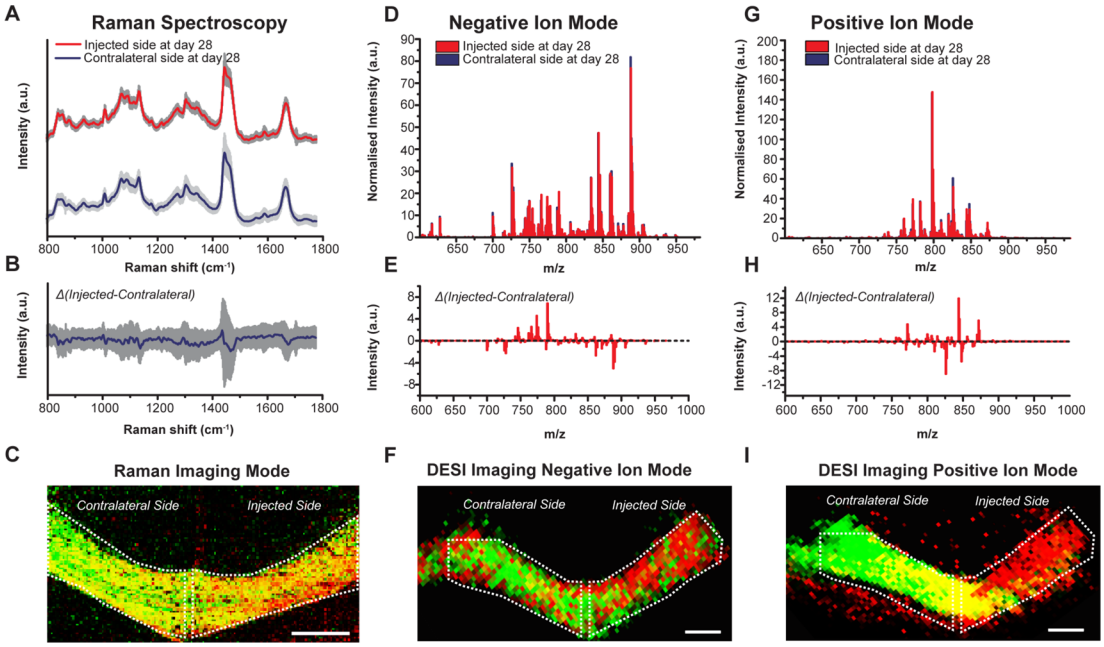

Figure 5. Heterospectral lipidomics of remyelinated lesions in a focal demyelination mouse model. (A, B) Mean Raman spectra ± 1 standard deviation (SD) of normal myelinated tissues (noninjected side) and remyelinated tissue (injected side, day 28 post toxin injection). (B) Mean difference spectra ± 1 SD (injected side, contralateral) showing the remyelination process at the structural level. (C) PLS-DA posterior probability image based on Raman spectroscopy of remyelinated sample discriminating control side (green) and injected side (red). Yellow represents nearly equal probability. (D, G) Mean DESI-MS mass spectra of normal myelinated tissues (noninjected side) and remyelinated tissue (injected side, day 28 post toxin injection) for negative and positive ion mode, respectively. (E, H) Mean difference spectra between remyelinated (day 28 post toxin injection) and control noninjected side for negative and positive ion mode, respectively. (F, I) MMC-LDA posterior probability based on DESI-MS negative ion mode and positive mode respectively belonging to control side (green) or injected side (red). Yellow represents nearly equal probability (images were rotated for presentation in this figure; originals are shown in Supplementary Figure S6D,E). Scale bar 250 μm.

demyelinated axons accounting for 90.68% (component 1, 61.55%, component 2, 29.13%, respectively) of the spectral variance. The omitted residual (7.39%) in the model was associated with artifacts from tissue preparation and cover glass background signal. Since MCR is based on spectral variance and because the amount of myelin lipids is the source of significant spectral variability in the image, MCR is able to estimate a spectrum of myelin lipids (Figure 4A). This is also evident by comparing the myelin signature with the pure lipids (Supplementary Figure S1) as well as the strong correlations in the heterospectral map (Figure 3D,E).

To validate the RMI for myelin quantification, we performed correlative immunohistochemistry for MBP and DAPI on the same tissues and used the immunofluorescence image to define injected and noninjected regions of interest (ROI) on each section (Supplementary Figure S3). These ROIs were then used to generate binary masks and extract the RMI. For this myelin quantification, the signal density from either MBP immunostaining or RMI images was calculated as a ratio of the signal density on the injected side of the corpus callosum compared to the noninjected side. The densitometry ratio of injected vs noninjected side for each sample was then normalized to the values obtained with control sections from untreated mice. We have summarized the average RMI ± 1 standard error (SE) at different time points (Figure 4C left panel). The results of this quantification showed a 52% reduction in myelin (0.50 fold decrease compared to 0.95 of control, ±0.14 fold change) at 14 days after injection compared to controls ($p < 0.05$). During remyelination, the RMI increased to 62% compared to the control untreated mice (0.61 fold decrease compared to 0.95 of control, ±0.12 fold change) at day 21 after lesion induction, and after 28 days the RMI progressively reverted back to control levels (0.96 fold decrease compared to 0.95 of control, ±0.03 fold change). These values correlated well with the MBP densitometric analysis performed on the correlative immunofluorescence images (Figure 4C central panel). The significant increase in $DAPI^+$ cells observed at day 14 after LPC injection (1.4 fold increase ± 0.13, $p < 0.05$) compared to control corresponds to an accumulation of microglia/macrophages in the lesion, which we identified by correlative immunofluorescence for the microglial marker IBA1 in a subset of sections already analyzed by Raman spectroscopy (Supplementary Figure S4). Along with the increased microglia/macrophage infiltration into demyelinated lesions, Raman spectroscopy also revealed the presence of cholesterol esters (through the presence of the ester vibrational mode at 1745 cm^{-1}), generally around the lesion site, suggestive of end products of myelin degradation, which is performed and then cleared by these cells.

We next assessed whether Raman analysis could identify specific biomolecular structural differences for different levels of myelination. We first calculated the mean Raman spectra ± 1 SD using the ROIs defined above as a guide (Figure 5A, Supplementary Figure S5A), and then we calculated the mean difference spectra for each time point to uncover subtle molecular differences between samples (Figure 5B, Supplementary Figure S5B). Spectral analysis showed that demyelinated lesions are associated with a distinct Raman spectroscopic profile, with reduction and/or spectral shifting in the peaks 1078, 1302, 1445, and 1650 cm^{-1}. Interestingly, there were spectral differences between normally myelinated and remyelinated tissue (day 28 post LPC injection). To investigate this

DOI: 10.1021/acscentsci.7b00367
ACS Cent. Sci. 2018, 4, 39−51

Table 1. DESI-MS Peak Annotation for Mouse Remyelinated Tissue[a]

m/z value	identification	ion type	accurate mass	fold change (remyelinated vs control)
		Positive Ion Mode		
770.49	PC (32:1)	$[M + K]^+$	770.5097	0.7367
848.53	PC (38:4)	$[M + K]^+$	848.5566	0.8416
826.56	PC (36:1)	$[M + K]^+$	826.5723	0.8531
810.58	PC (36:1)	$[M + Na]^+$	810.5983	0.8533
824.53	PC (36:2)	$[M + K]^+$	824.5566	0.8893
772.51	PC (32:0)	$[M + K]^+$	772.5253	1.1367
806.55	PC (32:3)	$[M + Na]^+$	806.567	1.4514
806.55	PC(38:3) or PC(40:6)	$[M + Na]^+$ or $[M + H]$	834.5983 or 834.6007	1.4527
806.55	PE (40:6)	$[M + Na]^+$	814.5357	1.4718
872.54	PC (40:6)	$[M + K]^+$	872.5566	1.5848
844.51	PC (38:6)	$[M + K]^+$	844.5253	1.6879
		Negative Ion Mode		
700.51	fragment of PE(34:1)	$PE(34:1) - NH_2 - H$	700.5049	0.8488
700.51	PE(20:4/16:0)	$[M - H]^-$	766.5392	1.1528
762.49	PE(16:0/22:6)	$[M - H]^-$	762.5079	1.3086
774.52	PE(16:0/22:6)	$[PE(40:6) - NH_2 - H]^-$	774.5205	1.3314
790.53	PE(18:0/22:6)	$[M - H]^-$	790.5392	1.4966

[a]The most significant mass spectrometry peaks in negative and positive ion mode identified using maximum margin criterion linear discriminant analysis (MMC-LDA) for discriminating between remyelinated and normal myelinated areas of the corpus callosum in the mouse model of toxin induced focal demyelination, confirmed by MSMS.

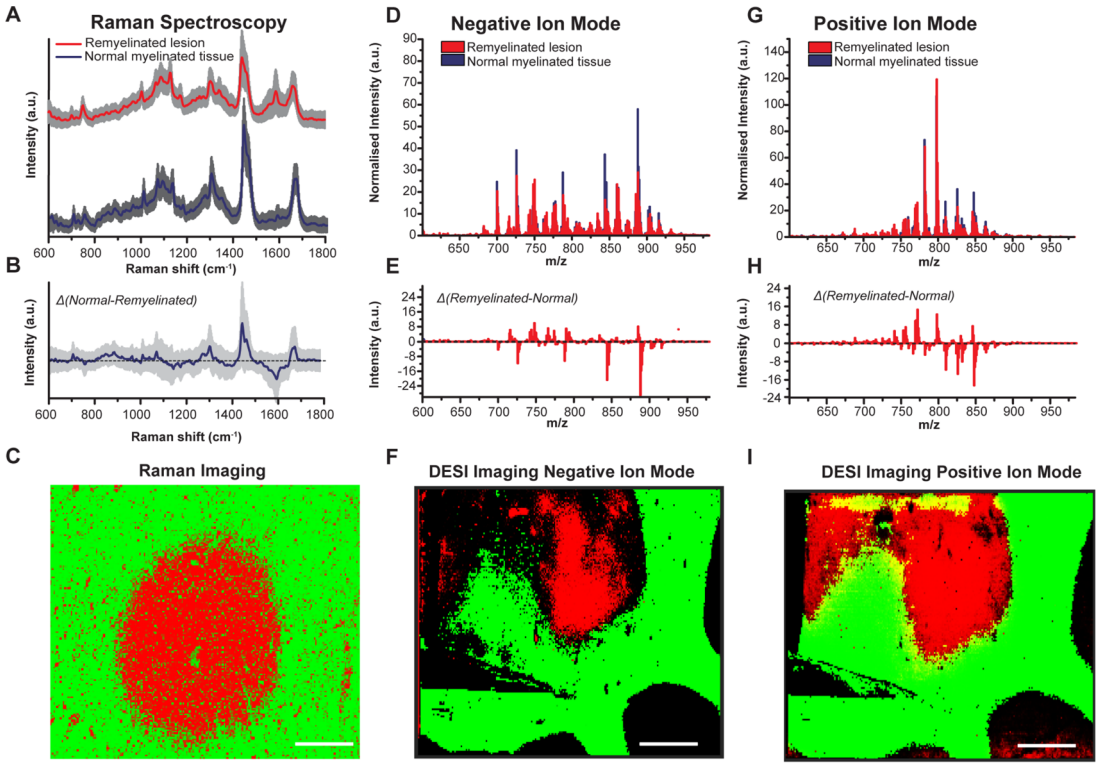

Figure 6. Heterospectral lipidomics of human multiple sclerosis brain. (A) Mean Raman spectra ± 1 standard deviation (SD) of normal appearing white matter (NAWM) and remyelinated lesions. (B) Mean difference spectra ± 1 SD (NAWM − remyelinated lesion) showing the remyelination process at the structural level. (C) PLS-DA posterior probability image based on Raman spectroscopy of remyelinated lesions highlighting NAWM (green) and remyelinated tissue (red). (D, G) Mean DESI-MS mass spectra of NAWM and remyelinated lesions for negative and positive ion mode, respectively. (E, H) Mean difference spectra between NAWM and remyelinated lesions for negative and positive ion mode respectively. (F, I) MMC-LDA posterior probability based on DESI-MS negative ion mode and positive mode respectively of belonging to NAWM (green) or remyelinated lesion (red). Yellow represents nearly equal probability. Scale bar 750 μm.

further, we performed PLS-DA on a day 28 tissue (remyelinated) compared to contralateral control and gray matter tissue. The 8 component PLS-DA accounted for 61.95% of the total variance where the first four latent variables (LVs) (LV1, 49.59%; LV2, 6.16%; LV3, 1.12%; and LV4, 1.77%) corresponded mostly to lipid peaks (e.g., CH_2 deformations at 1440 and C=C stretchings at 1650 cm^{-1}) (Supplementary Figure S6A and Figure 3D). Based on this analysis, we then

DOI: 10.1021/acscentsci.7b00367
ACS Cent. Sci. 2018, 4, 39−51

constructed an image of the corpus callosum that shows the probability of each pixel belonging to either the injected side (red) or noninjected side (green) (Figure 5C). These results show that newly formed myelin in remyelination can to some extent be distinguished from normal myelin using Raman imaging. The data presented thus far shows that Raman based characterization can detect subtle differences in the molecular structure of remyelinated and normal tissue.

The Raman myelination analysis was initially performed on fixed brain tissue. Since DESI-MS must be performed on fresh tissue, in addition, this allowed us to compare fixed and nonfixed brain to investigate potential differences introduced by the fixation process to the Raman profiling of brain tissue. The fixation process induces subtle molecular changes in the corpus callosum mostly around 1450 cm^{-1} associated with CH_2 deformations (Supplementary Figure S7), most likely due to conformational changes in proteins occurring during formaldehyde fixation. All subsequent Raman myelination analysis was performed on unfixed tissue, which was then immediately imaged with DESI-MS.

Following Raman spectroscopy, DESI-MS images were acquired from fresh mouse brain samples (remyelinated lesion (injected side at day 28) and contralateral normal side (noninjected side)). We calculated the average DESI mass spectra in the negative and positive ion modes (Figure 5D,G) as well as the mean difference spectra to highlight dissimilarities between the DESI mass spectra of the different samples (Figure 5E,H). To identify those masses that best differentiate remyelinated from control tissue, we performed MMC-LDA.[29] We calculated the MMC-LDA loading vectors for the negative and positive modes (Supplementary Figure S6B,C). We then produced images that show the posterior probability of belonging to the injected (red) or noninjected side (green). This analysis essentially confirmed the Raman spectral characterization and showed highly specific molecular changes in the remyelinated lesion (injected side) compared to the contralateral normal side (noninjected side), in particular for the positive ion mode (Figure 5F,I). The most significant peaks discriminating remyelinated and normal myelinated areas of the corpus callosum were then confirmed by tandem mass spectrometry (see Materials and Methods) and are reported in Table 1. The main differences between normal myelin and remyelinated tissue are generally due to changes in the composition of phosphatidylcholines (PCs) and phosphatidylethanolamines (PEs) within the analyzed areas. Hence, both the Raman and DESI-MS suggest that the lipid composition of remyelinated regions differs from that of original myelin. The results obtained from the mouse model serve as a proof of principle to show that HSL imaging can effectively investigate the lipidomic profile of remyelinated lesions, as well as providing the first direct indication that newly formed myelin after demyelination presents a distinct molecular signature and a relative lipid composition difference compared to normal myelin.

Application of Heterospectral Lipidomics to Multiple Sclerosis Patient Brain Samples. We finally applied our HSL approach to multiple sclerosis lesions from human *postmortem* brain samples for label-free lesion classification and lipidomic analysis. We obtained normal control brain samples (n = 4) and multiple sclerosis brain samples containing chronic active demyelinated lesions (n = 6), chronic inactive demyelinated lesions (n = 8), and remyelinated lesions (n = 4) from 8 multiple sclerosis patients. A total of 83,116 Raman spectra were measured from normal control tissue (n = 29,316 spectra), combined chronic active and inactive multiple sclerosis lesions (n = 14,354 spectra), and remyelinated lesions (n = 39,446 spectra) (Figure 6A and Supplementary Figure S8A). We calculated the difference spectra ± 1 SD to uncover the molecular differences associated with each tissue type (Figure 6B and Supplementary Figure S8B).

Although the pixelwise coregistrated HSL map we developed (Figure 3) was based on mouse tissue, it also informed our interpretation of the Raman spectra from human tissues. The multiple sclerosis remyelinated lesions showed less complete remyelination compared to the remyelination in the mouse model, as indicated by the lower intensity of lipid peaks at 1302, 1445, and 1650 cm^{-1}. There were also more pronounced peaks of mitochondria such as 1585 cm^{-1} associated with cellular infiltration of the lesion (Figure 6B). As in the mouse model, the Raman based analysis successfully identified specific signatures not only for demyelinated lesions but also for remyelinated lesions.

To further study these compositional differences, we performed correlative DESI-MS by comparing remyelinated lesions from 8 multiple sclerosis patient brains (identified by histopathological classification) with normal appearing white matter tissue from the same patient aiming to obtain the specific lipid profile associated with remyelinated lesions in patients (Figure 6D–I). We performed MMC-LDA to identify the most discriminative peaks that accounted for the differences observed between remyelinated and normal appearing white matter (Supplementary Figure S6C). The identified lipids were then confirmed by tandem mass spectrometry and are reported in Table 2. As observed in the mouse tissue analysis, the remyelinated areas differ mainly in the composition of the PC and PE lipid populations. These results indicate that HSL imaging can be effectively employed for lipidomic profiling of *postmortem* multiple sclerosis patient lesions, and suggest that the myelin produced during remyelination in multiple sclerosis has an altered lipid profile, when compared to nearby normal appearing white matter.

DISCUSSION

In this study, we developed a new heterospectral lipidomics (HSL) imaging method, for the classification and molecular characterization of myelination in both an animal model and human multiple sclerosis brain samples, and used it to directly observe for the first time that newly formed myelin is compositionally different from normal myelinated tissue. To harness the large amount of data generated, we developed a comprehensive computational library for correlative heterospectral imaging. The combined use of Raman spectroscopy and DESI-MS within the HSL workflow offers a simple and yet highly effective approach to profile the lipidomics of de- and remyelinated tissue at both the structural and compositional levels. In contrast to other techniques such as MALDI, our DESI-MS has the major advantage that it can be performed with no initial preparation on the same sample as for Raman spectroscopy thereby enabling true correlative analysis. Here we developed the first pixelwise coregistration approach for heterospectral Raman and DESI-MS imaging analysis. This allowed us to generate a correlation map that describes how the distinct vibrational molecular structural features correlate with compositional analysis. Further, we also showed for the first time that multivariate regression analysis between Raman spectra and mass spectra has the potential to enable Raman-

DOI: 10.1021/acscentsci.7b00367
ACS Cent. Sci. 2018, 4, 39–51

Table 2. DESI-MS Peak Annotation for Human Remyelinated Lesions[a]

m/z value	identification	ion type	accurate mass	fold change (remyelinated vs control)
		Positive Ion Mode		
848.53	PC (38:4)	$[M + K]^+$	848.5566	0.449
834.57	PC(38:3)	$[M + Na]^+$	834.5983	0.4628
814.51	PE (40:6)	$[M + Na]^+$	814.5357	0.4689
810.58	PC (36:1)	$[M + Na]^+$	814.5357	0.5674
826.56	PC (36:1)	$[M + K]^+$	826.5723	0.6284
824.53	PC (36:2)	$[M + K]^+$	824.5566	0.7083
806.49	PE (38:4)	$[M + K]^+$	806.5096	1.0512
872.54	PC (40:6)	$[M + K]^+$	872.5566	1.2509
844.51	PC (38:6)	$[M + K]^+$	844.5253	1.5723
770.49	PC (32:1)	$[M + K]^+$	770.5097	1.6884
772.51	PC (32:0)	$[M + K]^+$	772.5253	2.2756
		Negative Ion Mode		
762.49	PE(16:0/22:6)	$[M - H]^-$	762.5079	0.7603
700.51	PE(16:0/18:1)	$[PE(34:1) - NH_2 - H]^-$	700.5049	0.8252
790.53	PE(18:0/22:6)	$[M - H]^-$	790.5392	1.9916
774.52	fragment of PE(40:6)	$[PE(40:6) - NH_2 - H]^-$	774.5205	2.2611
774.52	fragment of PE(18:0/22:6)]	$[PE(40:6) - C_2H_4NH_2 - H]^-$	746.4892	2.4167
766.53	PE(20:4/16:0)	$[M - H]^-$	762.5392	3.0029

[a]The most significant mass spectrometry peaks in negative and positive ion mode identified using maximum margin criterion linear discriminant analysis (MMC-LDA) for discriminating between remyelinated and normal myelinated tissue in human brain samples, confirmed by MSMS.

based characterization of highly specific lipid species in complex tissue.

Our results indicate that Raman spectroscopy can discriminate between normal, demyelinated, and remyelinated areas in our mouse model and in human multiple sclerosis tissue, avoiding classical destructive and time-consuming analyses. In addition, we showed that Raman spectral analysis could identify structural differences not only between demyelinated and control tissue (comparable to that obtained with MBP staining), but importantly between control and remyelinated tissue, offering for the first time a specific comprehensive and distinct molecular signature for remyelinated tissue, with most of the differences in the lipid components. This concurs with previous knowledge that remyelinated and myelinated internodes have very similar protein components, but remyelinated myelin sheaths are thinner (due to less myelin wrapping).[30] The HSL correlation map enabled us to gain deeper insight into the biomolecular origin of the highly overlapping Raman peaks. Moreover, Raman spectroscopy enables a detailed structural molecular characterization of the tissue, as it not only can quantify the lipid component but also provides additional information on the underlying disease processes (such as immune infiltration, increased mitochondria, etc.) without requiring multiple immunostainings of serial histological sections.

Correlative DESI-MS analysis showed that some lipids can be over-represented in remyelinated myelin as well as under-represented, suggesting that remyelination can differ from normal myelin in more than simply a reduced amount of lipid secondary to a thinner sheath. PCs and PEs are two of the major constituents of mammalian cell membranes including those of myelin, and they account for most of the differences between remyelinated and normal myelin in both the mouse and human multiple sclerosis brains. In the focal demyelination mouse model, we found a trend toward decrease in some polyunsaturated PEs and PCs in remyelinated tissue, and a corresponding increase in PCs with higher saturation levels, which could correlate with the thinner myelin sheaths. In human remyelinated multiple sclerosis lesions we also observed a similar shift in several PC and PE species, but the exact changes are more complex to interpret. However, it is interesting to observe that both mouse and human remyelinated tissue showed an increase in PC(32:0), a phosphatidylcholine normally present in greater abundance within gray matter.[31] The reasons for some discrepancy between the remyelinated lesions in the mouse and human data sets may be due to intrinsic differences in lipid content in myelin between species, to interindividual/anatomical variations typical of patient samples. In fact, while in the mouse samples we had precise control over the anatomical area of the lesion (i.e., corpus callosum), the multiple sclerosis lesions came from different anatomical regions of the brain, and are certainly more heterogeneous than the murine samples along the remyelination timeline. However, given the scarcity of lipidomic data on myelin composition in health and pathology in both mouse and human, partially due to a previous lack of accessible and reliable techniques to perform these studies, we believe that these results offer an important, if preliminary, step toward a better understanding of remyelination, as they directly highlight previously unrecognized differences between myelin formed during endogenous regeneration and normal myelinated tissue. Using these techniques, and a bigger data set of patient samples, one will be able to address lipid variations in remyelinated multiple sclerosis lesions within a patient (removing genetic background variation) and between remyelinated lesions in similar locations between patients (reducing anatomical variation). Furthermore, as we know that myelin changes with age both at the ultrastructural level[32,33] and in terms of its lipid components,[34] this raises questions such as whether the lipid content of remyelinated myelin is more similar to young or old myelin, or different from both, and whether this changes in a similar way over time. Now that we have proof of principle that this strategy is suitable, we may answer these questions, both in animal models and by examining human multiple sclerosis samples of different ages, compared to controls of different ages. It is also important to determine whether the quality of remyelinated myelin is equivalent to normal myelin, whether it matures/ages at a different rate, and whether it can change in response to need, for example as required in activity-dependent myelination.[35] This has pertinence for the development of pro-remyelinating drugs as therapies in multiple sclerosis.

The HSL strategy developed here represents a powerful tool to classify, quantify, and analyze lipids in myelin, increasing information for selecting the most promising pro-remyelination therapeutic strategies. Understanding lipid structural and compositional differences between myelination and remyelination may allow us to identify remyelinated areas more efficiently. The HSL imaging workflow presented here will allow one to investigate specific questions such as whether these lipid differences alter the function of myelin, in terms of the efficiency of saltatory conduction and the metabolic support

DOI: 10.1021/acscentsci.7b00367
ACS Cent. Sci. 2018, 4, 39−51

to the underlying axon. In addition, future pragmatic studies could aim to apply simultaneous Raman and mass spectrometry for living tissue assessment as well as clinical applications toward lipidomic diagnostics. Both Raman spectroscopy and some mass spectroscopy approaches are in principle compatible with clinical applications.[36] Furthermore, the multivariate regression approach that we presented in this work can find widespread applications to uncover the plurality of molecular species in complex biological tissue.

In summary, we have developed a heterospectral lipidomics (HSL) methodology to quantify and characterize remyelination in a mouse model of induced focal demyelination and in human multiple sclerosis lesions. We demonstrated the first pixelwise coregistered heterospectral application of Raman spectroscopy and DESI-MS imaging. This analysis provides the first indication that newly formed myelin after demyelination has a different lipid composition compared to normal myelin. Hence, this HSL methodology may substantially improve the current understanding of remyelination in multiple sclerosis and may provide a new strategy to assess remyelination treatments in multiple sclerosis research. Furthermore, the HSL approach can be tailored to a broad range of tissues, providing crucial insights into lipid structure and composition in biomedical sciences.

MATERIALS AND METHODS

Animals. Animal work was carried out in accordance with the University of Edinburgh regulations under Home Office rules (PPL 60/4524), with local ethics committee consent. Animals were randomly allocated a treatment group.

Lesion Induction and Surgery. Myelin toxin lysophosphatidylcholine (LPC) was stereotactically injected into mouse corpus callosum to cause focal demyelination while leaving axons intact. The time course of demyelination and remyelination ensues in a stereotyped way, with a fully developed demyelinated lesion at 3 days post injection followed by spontaneous remyelination to completion in 4 weeks.[37] Using anesthetized 12−14-week-old C57Bl/6 male mice (n = 3 per time point), 2 μL of 1% (w/v) LPC (Sigma-Aldrich, UK) was injected through a hole drilled in the skull at stereotactic coordinates 1.2 mm posterior, 0.5 mm lateral, 1.4 mm deep to the bregma over 4 min using a 30 gauge needle attached to a Hamilton syringe, driven by a Nano pump (KD Scientific Inc., Holliston, MA), which was left *in situ* for 4 min to reduce backflow. A surgical sham control was also prepared by injecting phosphate-buffered saline (0.9% sodium chloride solution) in the same way. Mice were sacrificed at predefined time points (14, 21, and 28 days) post lesion induction.

Mice Tissue Section Preparation. Mice were terminally anesthetized and perfused transcardially either with 4% (w/v) paraformaldehyde (PFA) solution (for Raman analysis) or with phosphate-buffered saline (0.9% (w/v) sodium chloride solution) (for DESI analysis) at 14, 21, or 28 days post injection. For Raman analysis, brains were dissected and postfixed in 4% (w/v) PFA for a further 24 h, before immersion in increasing concentrations of sucrose solutions, and frozen in OCT embedding matrix. For DESI analysis, brains were flash frozen without fixation. Using a cryostat (Leica Inc. GmbH), 10 μm coronal sections were cut onto magnesium fluoride slides (Global Optics Ltd., UK) (Raman analysis) or Superfrost Plus (VWR International LLC Inc., Radnor, PA) adhesive glass slides (DESI analysis) and stored at −20 °C until use.

Human Brain Tissue Samples. *Postmortem* unfixed frozen tissue was obtained from the UK Multiple Sclerosis Tissue Bank via a UK prospective donor scheme with full ethical approval (MREC/02/2/39). Two independent researchers characterized the lesion types as chronic active, chronic inactive, or remyelinated using Luxol fast blue to detect myelin and Oil red O staining to detect macrophages/microglia.[11] Chronic active lesions have a demyelinated core with few inflammatory cells, but a ring of lipid-laden macrophages/microglia at their edge. Chronic inactive lesions have a sharp edge on LFB and few inflammatory cells throughout. Remyelinated lesions are filled with thin (pale-staining) myelin, with very few inflammatory cells remaining. We obtained normal control brain samples with no neurological disease (n = 4) and multiple sclerosis brain samples containing chronic active demyelinated lesions (n = 6), chronic inactive demyelinated lesions (n = 8), and remyelinated lesions (n = 4) from 8 different multiple sclerosis patients.

Reference Biochemicals. We constructed a spectral library of reference biochemicals representing the major proteins and lipids in CNS including MBP (M2941, Sigma-Aldrich (UK)), actin (C3653, Sigma-Aldrich (UK)), phosphatidylcholine (P3556), glycerophosphatidylcholine (S4335) sphingomyelin (860062, Avanti Polar Lipids Inc., Alabaster, AL), cholesterol (C8667, Sigma-Aldrich (UK)), DOPC (C8667, Sigma-Aldrich (UK)), galactocerebrosides (C4905, Sigma-Aldrich (UK)), cerebroside sulfate (S1006, Sigma-Aldrich (UK)), and LPC (L1381, Sigma-Aldrich (UK)). The Raman spectra of these reference biochemicals were all measured in native state on a magnesium fluoride (MgF_2) slide.

Raman Spectroscopy Imaging. The confocal Raman microspectroscopy system used in this study consists of an upright microscope (Alpha 3000, WITec, GmbH, Ulm) equipped with a piezoelectric stage (UHTS 300, WITec, GmbH, Ulm). A green laser (λ_{ex} = 532 nm, WITec GmbH, Ulm) with maximum output of 75 mW was fiber-coupled into the microscope using a 10 μm low OH silica fiber. The backscattered Raman signals were fed into a high-throughput imaging spectrograph (UHTS 300, WITec GmbH, Ulm), equipped with a thermoelectrically cooled (−60 °C), charge-coupled device (CCD) camera (Newton, Andor Technology Ltd., UK, Belfast) using a 100 μm low OH silica fiber. The system acquires Raman spectra in the range from 0 to 3600 cm^{-1} with a spectral resolution of ∼13 cm^{-1}.

For mice, Raman spectroscopy images (∼3000 × 1500 μm (spatial resolution of ∼6 μm)) were measured by raster scanning over contralateral regions of corpus callosum. Each Raman spectrum was collected with an acquisition time of ∼1.0 s and a power on the sample of ∼13 mW using the 532 nm laser excitation. No sample degradation due to heating was noticed using this power density. We did observe fluorescence bleaching for brain tissue using the 532 nm laser.

For human samples, Raman images were measured by raster scanning covering lesions and control tissue. We measured tissue from n = 8 patients. For each tissue/lesion we measured ∼2500 spectra in quadratic ROIs that each were 150 × 150 to 180 × 180 μm in size. Each Raman spectrum was collected with an acquisition time of ∼1.0 s and a power on the sample of ∼13 mW using the 532 nm laser excitation.

Raman Data Analysis. Before multivariate statistical analysis, the Raman spectra were preprocessed. First, to remove tissue autofluorescence, a constrained second-order polynomial was fitted to the raw spectrum in the range 500−3600 cm^{-1},

DOI: 10.1021/acscentsci.7b00367
ACS Cent. Sci. 2018, 4, 39−51

and this polynomial was then subtracted to yield the Raman spectrum alone. This was performed in the Project Four (WITec, Ulm, Germany). Each Raman spectrum was normalized to its total intensity. For univariate analysis we imaged the high wavenumber (due to higher signal intensity). For multivariate analysis and discrimination of subtle difference we analyzed the more specific fingerprint range.

Regions within the sample were annotated as either "control" or "lesion". These annotated pixels were extracted and analyzed using partial least-squares discriminant analysis (PLS-DA) and internal 10-fold cross validation.

k-means clustering ($n = 2$ clusters) was calculated in Project Four (WITec, Ulm, Germany) and used to coregister myelin lipids and MBP staining.

The Raman myelination index (RMI) was calculated using using non-negativity constrained MCR in the Matlab 2014b programming environment (MathWorks). All hyperspectral Raman images were combined into a single data set and analyzed together. A model complexity of three components essentially representing myelin, nonmyelinated tissue, and a residual (glass interference) provided an optimum molecular contrast of myelin in CNS tissue. The residuals were discarded and the two MCR components (myelin lipids and nonmyelinated tissue) were divided to form the RMI as a measure of the relative amount of myelin per axon area. All RMI values were normalized to the control hemisphere.

Immunohistochemistry. For immunostaining, brain slices were first treated with ice cold ethanol for 10 min for delipidation and then washed in PBS three times for 5 min, before addition of blocking solution (10% (v/v) donkey serum in TX-PBS 0.2% (v/v)). The primary antibodies (rat anti-MBP, Serotec Cat. No. MCA409S used at 1:200; mouse anti Beta3 Tubulin, Sigma-Aldrich Cat. No. T5076 used at 1:1000; goat anti-IBA1, Novus Cat. No. NB100-1028 used at 1:200) were added in blocking solution to each slide and incubated overnight at 4 °C. After the primary antibody incubation, the slides were washed in PBS three times for 5 min, before addition of the secondary antibody in blocking solution for 1.5 h. After the secondary incubation, the slides were incubated in a 1:5000 DAPI−PBS solution for 5 min before three final washes in TX-PBS 0.2% (v/v) before mounting. All antibodies were validated for specificity and background performing secondary only controls on additional mouse brain sections.

Raman and Immunofluorescence Coregistration. To enable correlative imaging, we then developed a comprehensive Matlab library for correlative Raman spectroscopy processing and immunofluorescence imaging. This library enables us to spatially overlay a database of Raman and immunofluorescence images and extract the average signature according to a used-defined ROI. Inverse trapezoidal ROIs of the left and right sides of the corpus callosum stained for MBP were defined in ImageJ and used to create bounding masks for the treated and control areas. The masked images were then linearly down sampled to match the resolution of the Raman spectroscopic images. Finally the masks were overlaid with the Raman spectroscopic images for correlative imaging using ImageJ. Quantification of myelination in brain sections for both RMI and MBP images was conducted by measuring the density of signal in the masked areas (noninjected side vs injected side), which was then divided by the area of the ROI. The measurements were then used to create a ratio of signal density between treated and untreated areas, which were then normalized on the values of control samples and expressed as fold change for the representation. Since for each condition we have 3 images, we pooled the RMI of the 3 replicates using only the pixels belonging to the same region, as inferred by the image registration. The control normalization was achieved by dividing all RMI values by the average value for the 3 control pooled replicates. Statistical analysis on the obtained data was performed using one-way ANOVA with Newman−Keuls post-test.

DESI-MS Imaging. Fresh frozen tissue sections were thawed at room temperature before being analyzed by DESI-MS. DESI-MS imaging was performed on a Xevo G2-XS quadrupole time-of-flight mass spectrometer (Waters Corporation, Milford, MA) equipped with a 2D DESI stage obtained from Prosolia Inc. (Indianapolis, IN), and a custom-built inlet capillary heated to 490 °C. DESI parameters were optimized for best spatial resolution on tissue and were as follows: spray voltage, 4.5 kV; solvent, methanol/water, 95:5; flow rate, 0.5 μL/min; nebulizing gas, nitrogen; gas pressure, 4 bar; sprayer incidence angle, 75°; collection angle, 10°; sprayer-to-inlet distance, 8 mm; sprayer-to-sample distance, 0.5 mm. Mass spectrometric parameters were as follows: source temperature, 120 °C; source offset, −80 V; 4 scans/s. Mouse brain samples were imaged at a nominal pixel size of 25 μm; the full mouse brain sample (Figure 2G) and human brain samples were imaged at a nominal pixel size of 50 μm.

MSMS Fragmentation. To identify the significant features, MSMS fragmentation was performed using a LTQ Orbitrap Discovery (Thermo Fischer Scientific Inc., Waltham, MA, USA) linear ion trap equipped with a home-built computer controlled 2D sampling stage and DESI-sprayer. The sprayer voltage was set to 4.5 kV for both positive and negative acquisition modes. A mixture of methanol/water (95%/5%) was delivered with a flow rate of 1.5 μL/min and nebulized with a N_2 gas pressure of 6 bar. Spectra were isolated from line scans across a mouse brain section performed with a sample moving speed of 50 μm/s. The identification of positive mode MSMS fragments was performed by matching the fragmentation patterns of the compounds analyzed with previously reported fragmentation pattern for PCs and PEs.[38] The identification of negative mode MSMS fragments was mainly based on the mass of fatty acid carboxylate fragments. For all features, the accurate mass was compared to the measured mass and compounds. All compounds with a mass difference of more than 25 ppm were excluded. Whenever possible, the acquired spectra were also compared to the MSMS fragmentation pattern provided in the Metlin database (https://metlin.scripps.edu).

DESI-MS Data Analysis. Mass spectrometry imaging data were imported into the Matlab (Mathworks Inc., Natick, MA, USA) environment and processed using an in-house toolbox.[29,39] Regions within each sample were annotated as either "control" or "lesion". These annotated pixels across the sample cohort were extracted and binned to 1 Da resolution over the (phospholipid) m/z range 600−1000. Each spectrum was normalized to its total intensity.

One-way analysis of variance (ANOVA) was performed between control and lesion groups. False discovery rate (FDR) correction was applied using the Benjamini−Hochberg−Yekutieli (BHY) method with $\alpha = 0.05$. Principal component analysis (PCA) was used to identify trends in the data, and maximum margin criterion linear discriminant analysis (MMC-LDA) was used to classify control and lesion spectra. For MMC-LDA, a 10-fold internal cross validation scheme was employed. Accurate masses and annotations of significant

DOI: 10.1021/acscentsci.7b00367
ACS Cent. Sci. 2018, 4, 39−51

features were determined by reference to the tandem MS experiments. Annotation of the top ten most differentiating peaks for each group and ion mode was performed using the Lipid Maps (http://www.lipidmaps.org/) and METLIN (https://metlin.scripps.edu/index.php) databases and a mass accuracy of 15 ppm.

Raman and DESI-MS Coregistration and Heterospectral Analysis. The mouse samples analyzed by DESI (negative mode) and Raman were coregistered using a fiducial marker-based alignment. Four pairs of corresponding markers were manually marked on each of the two images. An affine transformation was used to coregister the DESI image to match the Raman image. Each of the individual DESI ion images was resized and linearly interpolated using the imwarp function in Matlab (Mathworks Inc., Natick, MA, USA). Following coregistration, a single region spanning the corpus callosum and "background" was marked, with these pixels from DESI and Raman being unit vector normalized prior to correlation analysis.[40] Correlation coefficients between DESI and Raman variables were determined. Correlations with $p > 0.05$ were discounted. Finally, we also performed a multivariate regression analysis of the normalized Raman spectra against the individual masses using a 3 component PLS regression with venetian blind cross validation to estimate model complexity.

Data Availability. Supporting raw data is available at DOI: https://doi.org/10.5281/zenodo.1064450.

■ ASSOCIATED CONTENT

Supporting Information

The Supporting Information is available free of charge on the ACS Publications website at DOI: 10.1021/acscentsci.7b00367.

Raman spectral library of major CNS myelin components and additional Raman studies (PDF)

■ AUTHOR INFORMATION

Corresponding Authors

*E-mail: m.stevens@imperial.ac.uk.
*E-mail: anna.williams@ed.ac.uk.
*E-mail: z.takats@imperial.ac.uk.

ORCID

Andrea Serio: 0000-0002-7271-1878
James S. McKenzie: 0000-0002-1007-317X
Ciro Chiappini: 0000-0002-9893-4359
Zoltan Takats: 0000-0002-0795-3467
Molly M. Stevens: 0000-0002-7335-266X

Present Address

[⊥]A.S.: Division of Tissue Engineering & Biophotonics, King's College London, London SE1 9RT, United Kingdom. C.C.: Department of Craniofacial Development and Stem Cell Biology, King's College London, London SE1 9RT, United Kingdom

Author Contributions

[‖]M.S.B. and A.S. contributed equally to the work. M.S.B. and A.S. designed the study, interpreted the data, generated the figures, and wrote the manuscript. M.S.B. and A.S conducted Raman spectroscopy, correlative immunofluorescence work, and data analyses. J.T., V.W, and A.D. performed DESI-MS, and J.S.M. conducted DESI-MS data analysis supervised by Z.T. A.B. and A.W. performed the animal surgery, tissue sample preparation, and histological evaluation. C.C. contributed to scientific discussion, study design, and interpretation of the data. Z.T., A.W., and M.M.S. contributed to the study design, data interpretation, and scientific discussions and revised the manuscript. M.M.S supervised the study.

Notes

The authors declare no competing financial interest.

■ ACKNOWLEDGMENTS

We acknowledge the support of the UK Regenerative Medicine Platform grants "Acellular Approaches for Therapeutic Delivery" (MR/K026682/1) and "A Hub for Engineering and Exploiting the Stem Cell Niche" (MR/K026666/1). M.M.S. acknowledges the grant "State of the Art Biomaterials Development and Characterisation of the Cell-Biomaterial Interface" (MR/L012677/1) from the MRC. M.S.B. acknowledges support from H2020 through the Individual Marie Skłodowska-Curie Fellowship "IMAGINE" (701713). This research was also funded by Waters Corporation and supported by the European Union Seventh Framework Programme (FP7/2007−2013 under Grant Agreement No. 297499/305940), and the European Research Council Consolidator Grant, Grant Agreement No. 617896.

■ REFERENCES

(1) Huxley, A. F.; Stämpfli, R. Evidence for saltatory conduction in peripheral myelinated nerve fibres. *J. Physiol. (Oxford, U. K.)* **1949**, *108*, 315−339.
(2) Fünfschilling, U.; et al. Glycolytic oligodendrocytes maintain myelin and long-term axonal integrity. *Nature* **2012**, *485*, 517−521.
(3) Lee, Y.; et al. Oligodendroglia metabolically support axons and contribute to neurodegeneration. *Nature* **2012**, *487*, 443−448.
(4) Huang, J. K.; et al. Myelin regeneration in multiple sclerosis: targeting endogenous stem cells. *Neurotherapeutics* **2011**, *8*, 650−658.
(5) Hampton, D. W.; et al. Neurodegeneration progresses despite complete elimination of clinical relapses in a mouse model of multiple sclerosis. *Acta Neuropathol Commun.* **2013**, *1*, 84.
(6) Goldschmidt, T.; Antel, J.; König, F. B.; Brück, W.; Kuhlmann, T. Remyelination capacity of the MS brain decreases with disease chronicity. *Neurology* **2009**, *72*, 1914−1921.
(7) Bramow, S.; et al. Demyelination versus remyelination in progressive multiple sclerosis. *Brain* **2010**, *133*, 2983−2998.
(8) Patani, R.; Balaratnam, M.; Vora, A.; Reynolds, R. Remyelination can be extensive in multiple sclerosis despite a long disease course. *Neuropathol. Appl. Neurobiol.* **2007**, *33*, 277−287.
(9) Patrikios, P.; et al. Remyelination is extensive in a subset of multiple sclerosis patients. *Brain* **2006**, *129*, 3165−3172.
(10) Zhang, H.; Jarjour, A. A.; Boyd, A.; Williams, A. Central nervous system remyelination in culture−a tool for multiple sclerosis research. *Exp. Neurol.* **2011**, *230*, 138−148.
(11) Boyd, A.; Zhang, H.; Williams, A. Insufficient OPC migration into demyelinated lesions is a cause of poor remyelination in MS and mouse models. *Acta Neuropathol.* **2013**, *125*, 841−859.
(12) Huang, J. K.; et al. Retinoid X receptor gamma signaling accelerates CNS remyelination. *Nat. Neurosci.* **2011**, *14*, 45−53.
(13) Lappe-Siefke, C.; et al. Disruption of Cnp1 uncouples oligodendroglial functions in axonal support and myelination. *Nat. Genet.* **2003**, *33*, 366−374.
(14) Griffiths, I.; et al. Axonal swellings and degeneration in mice lacking the major proteolipid of myelin. *Science* **1998**, *280*, 1610−1613.
(15) Manrique-Hoyos, N.; et al. Late motor decline after accomplished remyelination: Impact for progressive multiple sclerosis. *Ann. Neurol.* **2012**, *71*, 227−244.
(16) Bambery, K. R.; Wood, B. R.; McNaughton, D. Resonant Mie scattering (RMieS) correction applied to FTIR images of biological tissue samples. *Analyst* **2012**, *137*, 126−132.

DOI: 10.1021/acscentsci.7b00367
ACS Cent. Sci. 2018, 4, 39−51

(17) Krafft, C.; Kirsch, M.; Beleites, C.; Schackert, G.; Salzer, R. Methodology for fiber-optic Raman mapping and FTIR imaging of metastases in mouse brains. *Anal. Bioanal. Chem.* **2007**, *389*, 1133−1142.
(18) Shi, Y.; et al. Longitudinal in vivo coherent anti-Stokes Raman scattering imaging of demyelination and remyelination in injured spinal cord. *J. Biomed. Opt.* **2011**, *16*, 106012.
(19) Ayala, G.; Carmona, P.; de Cózar, M.; Monreal, J. Vibrational spectra and structure of myelin membranes. *Eur. Biophys. J.* **1987**, *14*, 219−225.
(20) Krafft, C.; Neudert, L.; Simat, T.; Salzer, R. Near infrared Raman spectra of human brain lipids. *Spectrochim. Acta, Part A* **2005**, *61*, 1529−1535.
(21) Vanrobaeys, F.; Van Coster, R.; Dhondt, G.; Devreese, B.; Van Beeumen, J. Profiling of Myelin Proteins by 2D-Gel Electrophoresis and Multidimensional Liquid Chromatography Coupled to MALDI TOF−TOF Mass Spectrometry. *J. Proteome Res.* **2005**, *4*, 2283−2293.
(22) Bocklitz, T. W.; et al. Deeper understanding of biological tissue: quantitative correlation of MALDI-TOF and Raman imaging. *Anal. Chem.* **2013**, *85*, 10829−10834.
(23) Ahlf, D. R.; Masyuko, R. N.; Hummon, A. B.; Bohn, P. W. Correlated mass spectrometry imaging and confocal Raman microscopy for studies of three-dimensional cell culture sections. *Analyst* **2014**, *139*, 4578−4585.
(24) Lasch, P.; Noda, I. Two-Dimensional Correlation Spectroscopy for Multimodal Analysis of FT-IR, Raman, and MALDI-TOF MS Hyperspectral Images with Hamster Brain Tissue. *Anal. Chem.* **2017**, *89*, 5008−5016.
(25) Vickerman, J. C. Molecular imaging and depth profiling by mass spectrometry—SIMS, MALDI or DESI? *Analyst* **2011**, *136*, 2199−19.
(26) Eberlin, L. S.; Ferreira, C. R.; Dill, A. L.; Ifa, D. R.; Cooks, R. G. Desorption electrospray ionization mass spectrometry for lipid characterization and biological tissue imaging. *Biochim. Biophys. Acta, Mol. Cell Biol. Lipids* **2011**, *1811*, 946−960.
(27) Felten, J.; et al. Vibrational spectroscopic image analysis of biological material using multivariate curve resolution-alternating least squares (MCR-ALS). *Nat. Protoc.* **2015**, *10*, 217−240.
(28) Bergholt, M. S.; et al. Raman Spectroscopy Reveals New Insights into the Zonal Organization of Native and Tissue-Engineered Articular Cartilage. *ACS Cent. Sci.* **2016**, *2*, 885−895.
(29) Veselkov, K. A.; et al. Chemo-informatic strategy for imaging mass spectrometry-based hyperspectral profiling of lipid signatures in colorectal cancer. *Proc. Natl. Acad. Sci. U. S. A.* **2014**, *111*, 1216−1221.
(30) Harrison, B. M.; McDonald, W. I. Remyelination after transient experimental compression of the spinal cord. *Ann. Neurol.* **1977**, *1*, 542−551.
(31) Jarmusch, A. K.; et al. Differential Lipid Profiles of Normal Human Brain Matter and Gliomas by Positive and Negative Mode Desorption Electrospray Ionization − Mass Spectrometry Imaging. *PLoS One* **2016**, *11*, e0163180.
(32) Safaiyan, S.; et al. Age-related myelin degradation burdens the clearance function of microglia during aging. *Nat. Neurosci.* **2016**, *19*, 995−998.
(33) Xie, F.; Liang, P.; Fu, H.; Zhang, J.-C.; Chen, J. Effects of normal aging on myelin sheath ultrastructures in the somatic sensorimotor system of rats. *Mol. Med. Rep.* **2014**, *10*, 459−466.
(34) Ando, S.; Tanaka, Y.; Toyoda, Y.; Kon, K. Turnover of myelin lipids in aging brain. *Neurochem. Res.* **2003**, *28*, 5−13.
(35) Bechler, M. E.; Swire, M.; ffrench-Constant, C. Intrinsic and adaptive myelination-A sequential mechanism for smart wiring in the brain. *Dev. Neurobiol.* **2017**, DOI: 10.1002/dneu.22518.
(36) Alexander, J.; et al. A novel methodology for in vivo endoscopic phenotyping of colorectal cancer based on real-time analysis of the mucosal lipidome: a prospective observational study of the iKnife. *Surg Endosc* **2017**, *31*, 1361−1370.
(37) Woodruff, R. H.; Fruttiger, M.; Richardson, W. D.; Franklin, R. J. M. Platelet-derived growth factor regulates oligodendrocyte progenitor numbers in adult CNS and their response following CNS demyelination. *Mol. Cell. Neurosci.* **2004**, *25*, 252−262.
(38) Nilsson, A.; et al. Fine mapping the spatial distribution and concentration of unlabeled drugs within tissue micro-compartments using imaging mass spectrometry. *PLoS One* **2010**, *5*, e11411.
(39) Tillner, J.; et al. Investigation of the Impact of Desorption Electrospray Ionization Sprayer Geometry on Its Performance in Imaging of Biological Tissue. *Anal. Chem.* **2016**, *88*, 4808−4816.
(40) Crockford, D. J.; et al. Statistical heterospectroscopy, an approach to the integrated analysis of NMR and UPLC-MS data sets: application in metabonomic toxicology studies. *Anal. Chem.* **2006**, *78*, 363−371.

DOI: 10.1021/acscentsci.7b00367
ACS Cent. Sci. 2018, 4, 39−51